

Signatures of spinon dynamics and phase structure of dipolar-octupolar quantum spin ices in two-dimensional coherent spectroscopy

Mark Potts,¹ Roderich Moessner,¹ and Owen Benton^{1,2}

¹Max Planck Institute for the Physics of Complex Systems, Nöthnitzer Str. 38, Dresden 01187, Germany

²School of Physical and Chemical Sciences, Queen Mary University of London, London, E1 4NS, United Kingdom

(Dated: June 4, 2024)

We study how sharp signatures of fractionalization emerge in nonlinear spectroscopy experiments on spin liquids with separated energy scales. Our model is that of dipolar-octupolar rare earth pyrochlore materials, prime candidates for realising quantum spin ice. This family of three dimensional quantum spin liquids exhibits fractionalization of spin degrees of freedom into spinons charged under an emergent $U(1)$ gauge field. We show that the technique of two dimensional coherent spectroscopy (2DCS) can identify clear signatures of fractionalised spinon dynamics in dipolar-octupolar quantum spin ices. However, at intermediate temperatures, spinon dynamics are heavily constrained in the presence of an incoherent spin background, leading to a *broad* 2DCS response. At lower temperatures, a sharp signal emerges as the system enters a coherent spin liquid state. This lower temperature signal can in turn distinguish between zero-flux and π -flux forms of quantum spin ice.

The emergence of fractional excitations [1, 2] is a feature of many exotic quantum states, including quantum spin liquids [3–6] and topologically ordered phases of matter [7, 8]. Establishing clear signatures of such excitations is then key to the unambiguous identification of these phases in real materials. Fractional excitations can only be created in multiplets, and never singly, meaning that, from kinematic considerations, linear response functions are broad. These broad responses are difficult to unambiguously distinguish from the response of conventional excitations broadened by (e.g.) disorder or finite lifetime effects.

The technique of two-dimensional coherent spectroscopy (2DCS) [9–11] has been proposed as a method that avoids this issue. 2DCS is a non-linear optical technique which produces responses that are functions of two frequencies ω_t and ω_r . The continuum response from the excitation of zero-momentum pairs of fractionalised excitations becomes a sharp extended signal along the $\omega_t = -\omega_r$ line in the two-dimensional frequency plane, termed the ‘spinon-echo’ or ‘rephasing’ signal. The effects of disorder, or the finite lifetime of quasiparticles, are responsible for any broadening of the signal transverse to this line, allowing the existence of a continuum from fractionalized excitations to be distinguished from these other effects.

The technique has been investigated theoretically in a number of settings [9, 12–14], though primarily in exactly solvable models such as the Kitaev honeycomb spin liquid, or certain one dimensional models. Here, we discuss the application of 2DCS to quantum spin ice (QSI) - a class of three dimensional spin liquids on the pyrochlore lattice [15–19]. In recent years several materials have been suggested as promising candidates for systems with QSI ground states [19–25], although definitively establishing the presence of such a spin liquid in any specific material remains challenging.

The most promising QSI candidate materials have been the rare earth pyrochlores, in particular the Ce based

materials $\text{Ce}_2\text{Zr}_2\text{O}_7$, $\text{Ce}_2\text{Sn}_2\text{O}_7$ and $\text{Ce}_2\text{Hf}_2\text{O}_7$ [22–28]. These are all examples of so-called dipolar-octupolar pyrochlores due to the particular symmetry properties of their pseudospin-1/2 magnetic degrees of freedom.

In this Letter we discuss the capacity of 2DCS to identify fractionalised excitations within QSI phases. We present a theory for the 2DCS of dipolar-octupolar pyrochlores in two settings: (i) an intermediate temperature regime where spinon excitations are quantum coherent, but the initial state of the system can be taken to be an incoherent ensemble of classical spin ice ground states, which is treated using degenerate perturbation theory and exact diagonalization; (ii) the low energy regime where quantum coherence between spin ice states is important, which is treated using a gauge mean field theory (GMFT) [18, 29–31].

We demonstrate that the 2DCS response produces a (perhaps surprising) broad response in the intermediate temperature regime [Fig. 1], as the incoherent spin background constrains the motion of spinon excitations such that they no longer possess a well defined real-space momentum. Instead, their dynamics can be approximated by motion on a Husimi cactus graph [Fig. 2], with respect to which spinons have a well defined pseudo-momentum. Due to geometrical coupling factors between the field and local magnetic moments, the probe field does not conserve this pseudo-momentum, resulting in a broad signal in the 2DCS response.

By contrast, in the low temperature regime, the ground state is expected to be a coherent superposition of classical ice states, removing the constraints on spinon motion, and allowing spinons to acquire a definite real-space momentum. Sharp features are thus obtained in the 2DCS response, distinguishing this regime from the higher temperature regime [Fig. 3]. Further, we show that the 2DCS response can clearly discriminate between the two possible quantum spin ice phases predicted for dipolar-octupolar pyrochlores in GMFT, the 0-flux and π -flux $U(1)$ QSLs. In the π -flux phase, an increased unit cell size results in

multiple spinon bands [31], and transitions between these bands produce streaks away from the main rephasing diagonal in the 2DCS response.

Following a brief overview of dipolar-octupolar pyrochlores, we will discuss these items in turn. The most general nearest neighbour Hamiltonian for dipolar-octupolar pyrochlores is [31, 32]:

$$H = \sum_{\langle i,j \rangle} J_{yy} S_i^y S_j^y - J_{\pm} (S_i^+ S_j^- + S_i^- S_j^+) + J_{\pm\pm} (S_i^+ S_j^+ + S_i^- S_j^-), \quad (1)$$

with $\langle i, j \rangle$ denoting nearest neighbour sites on the pyrochlore lattice, and the ladder operators being defined relative to the y direction of pseudospin space. Motivated by the estimated parameter ranges for Ce pyrochlores [23, 25, 33], we assume that the dominant coupling is $J_{yy} > 0$. The S_j^μ operators are pseudo-spin operators acting in the lowest energy Kramers doublet of the magnetic ions. Under the action of the point group of the lattice and time reversal, the S^z and S^x pseudo-spin operators transform as magnetic dipoles, whilst S^y transforms as a magnetic octupole [32, 34]. For the basis chosen for Eq. (1), the dipolar coupling between the magnetic degrees of freedom and an external probe field \mathbf{H} is given by: $\mu_{BGz} \mathbf{H} \cdot \mathbf{z}_i (\cos \theta S_i^z + \sin \theta S_i^x)$. Here θ is a material dependent parameter, and the \mathbf{z}_i are unit vectors directed along the lines connecting the centres of neighbouring tetrahedra on the pyrochlore lattice. These tetrahedra sit on two fcc sublattices, which we define as the ‘A’ and ‘B’ sublattices. This geometrical coupling factor between the external field and local degrees of freedom endows the probe field operator with some site dependence, which we find has a significant effect on the linear and non-linear responses of the system.

The rephasing signal that we calculate is only part of the full 2DCS response [9], and is obtained from the imaginary part of the Fourier transform of the non-linear susceptibility $\chi^{(3)}(t, t, t + \tau)$:

$$\frac{i^3 \theta(t) \theta(\tau)}{N} \langle [M(t + \tau), M(\tau)], M(\tau)], M(0) \rangle, \quad (2)$$

with $M(t)$ the time-dependent operator coupling the probe field and the pseudo-spin degrees of freedom.

Intermediate temperature regime- In the limit of large J_{yy} , the Hamiltonian of Eq. (1) can be treated in degenerate perturbation theory. The low energy states then obey a ‘2-in-2-out’ ice rule on S_i^y – making the system an octupolar spin ice. Tunnelling between such configurations happens perturbatively and is of order $\sim |J_{\pm}|^3 / J_{yy}^2$, while local violations of the ice rule (spinons) hop with matrix element $\sim J_{\pm}$.

At intermediate temperatures such that $|J_{\pm}|^3 / J_{yy}^2, |J_{\pm\pm}|^3 / J_{yy}^2 \ll T \ll |J_{\pm}|$, only the first order spinon hopping will be relevant, and the equilibrium state will be an incoherent ensemble of classical spin ice states. A schematic of the spinon hopping generated by the J_{\pm} effective Hamiltonian is presented in Fig. 2. Note that this term in the Hamiltonian is symmetric

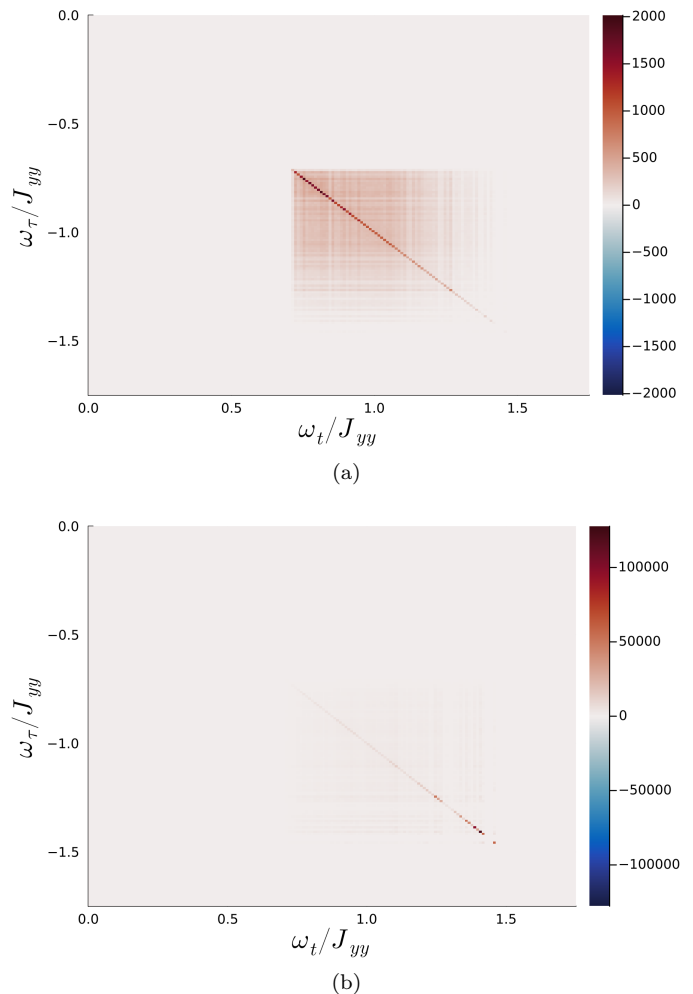


FIG. 1. 2DCS response of dipolar-octupolar QSI in the intermediate temperature regime with ((a)) and without ((b)) the geometrical factors $\mathbf{H} \cdot \mathbf{z}_i$ included in the field probe operator, as calculated using exact diagonalization on a finite cluster of 32 sites. A significant broad signal is observed if the correct geometrical coupling factors are included, due to the failure of the probe field operator to conserve the spinons’ pseudo-momentum. By contrast, a much sharper rephasing streak is observed if the probe is modified to conserve pseudo-momentum by removing site dependent factors. The spectral weight of the response is shifted to the upper end of the spinon band, which can be understood in terms of an effective pseudo-momentum vertex factor (supplementary material [35]) In both cases $J_{\pm} = -0.1, J_{yy} = 2$, and the Lorentzian linewidth $\Gamma = 0.001$

under rotations in the S^x, S^z plane, and so we can freely set θ to zero.

To obtain the 2DCS response of the system in this regime, the J_{\pm} perturbation (the second term in Eq. (1)) is exactly diagonalized in the two and four spinon sectors on a 32-site cluster of the pyrochlore lattice. The calculated 2DCS response in this regime is presented in the first panel of Fig. 1. Whilst a streak resembling the expected response for a system with fractionalised

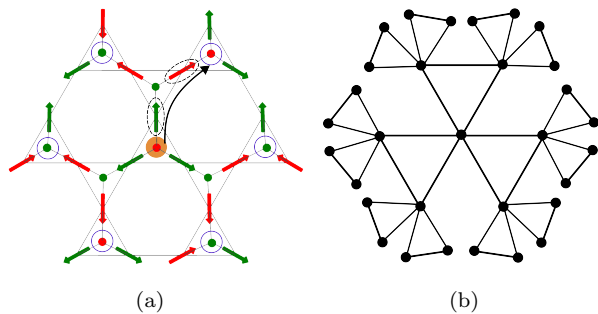


FIG. 2. (a) Section of the pyrochlore lattice with a single spinon indicated with a full orange circle. Each tetrahedron has 12 nearest neighbour tetrahedra on the same fcc sublattice, however the constrained hopping introduced in first order degenerate perturbation theory only allows the spinon to hop to the six sites indicated with empty blue circles. (b): The Husimi cactus approximation for the many-body state space of a single spinon. Each state is connected to six other states, and the system can return to the same state via cycles of 3.

excitations is observed, it is accompanied by a broad region of non-zero intensity, which is unexpected for a system possessing coherent fractionalised excitations.

We can understand the broad response obtained by making use of an approximate analytic treatment of the spinon dynamics, wherein spinon dynamics are modelled using a Bethe lattice-like graph.

To motivate this, we first note that the hopping generated by the perturbation Hamiltonian does not allow spinons to freely move across the lattice. A spinon on the ‘A’ fcc sublattice of tetrahedra will always remain on the ‘A’ sublattice. Moreover, a spinon must hop by flipping two neighbouring spins of opposite sign or of opposite colour in Fig. 2 (into or out of an ‘A’ tetrahedron), and must not generate any further violations of the ice rule as they move. This allows spinons to access only 6 of the 12 nearest neighbour fcc sites in a single hop, with these 6 sites dependent on the local spin configuration.

There are interaction effects between spinons: spinons flip spins as they move, which then influences the paths other spinons can take across the pyrochlore lattice; neighbouring spinons that share a majority spin on their respective tetrahedra impose further restrictions on the number of states the other can hop to [36].

One of the most important aspects of the dynamics is that if a spinon traverses a closed loop on the fcc lattice, it may leave a loop of flipped spins in its wake, meaning that the system has not returned to the same many-body state, and thus this process does not correspond to a closed loop on a graph of the many-body states of the system.

We consider such a graph in more detail for the hopping of one isolated spinon. If each state is a vertex on this graph, it is then connected to 6 other vertices. Spinons can hop in 3-cycles on the fcc lattice in such a way that the background spin configuration is unchanged, meaning

that these are also loops in the many-body graph. The graph is then approximately a tree of triangles, with three triangles attached to each vertex. The many-body state graph will have other larger loops (of six hops or larger), corresponding to the double traversal of loops on the fcc lattice with spins connected ‘head to tail’. As the presence of these larger loops depends on the local spin configuration, they do not appear uniformly across the graph, and so the tree of triangles, or cactus, is a reasonable approximation to the state graph for single spinon hopping.

The resulting Husimi cactus graph is presented in the second panel of Fig. 2, as described in Ref. [36]. Within this approximation, spinon dynamics undergo an effective dimension reduction, and obtain a one-dimensional dispersion indexed by a pseudo-momentum p . This model for the spinon dynamics has been shown to successfully reproduce the linear responses of QSI within this temperature regime [36] when compared with exact diagonalization, *a posteriori* justifying its use.

From the Husimi cactus viewpoint, we can explain the broad features observed in the 2DCS response of Fig. 1. The probe field operator $M(t)$ is proportional to $\sum_i \mathbf{H} \cdot \mathbf{z}_i S_i^z$ for dipolar-octupolar pyrochlores. The spatial dependence of this coupling prevents $M(t)$ from conserving spinon pseudo-momentum on the Husimi cactus. Without the conservation of pseudo-momentum, the ‘rephasing’ that occurs in Eq. (2) to ensure a sharp streak response along $\omega_t = -\omega_\tau$ fails, and a broad response results. Further details concerning the representation of the probe field operator $M(t)$ in the Husimi cactus picture, and a demonstration that it does not conserve pseudo-momentum is presented in supplementary material [35].

That the broad response is a direct consequence of the pseudo-momentum non-conservation is verified by modifying the probe field operator such that it has a definite pseudo-momentum. This is achieved by replacing the $\mathbf{H} \cdot \mathbf{z}_i$ coupling factors with a uniform constant \mathbf{H} to remove any site dependence from $M(t)$. Using this operator, we find that the computed 2DCS response has a sharp rephasing streak, as shown in the second panel of Fig. 1, supporting the conclusion that the broad features in the 2DCS response in the intermediate temperature regime as calculated for the realistic probe field operator are indicative of the constrained spinon dynamics.

Low temperature regime- The 2DCS response has significant broad features when quantum coherence between classical spin-ice states is suppressed by thermal fluctuations. If instead we work in a $T = 0$ limit, this anomalous broadening is removed, and characteristic sharp rephasing signals are recovered. In this limit, both the gauge field and spinon degrees of freedom are quantum coherent. We analyse this regime of the problem by appealing to gauge mean field theory, making use of the formulation described in Ref. [31]. By the nature of mean field theories, this calculation is less controlled than the exact diagonalization analysis used in the intermediate temperature regime, however we expect it to still provide a useful qualitative

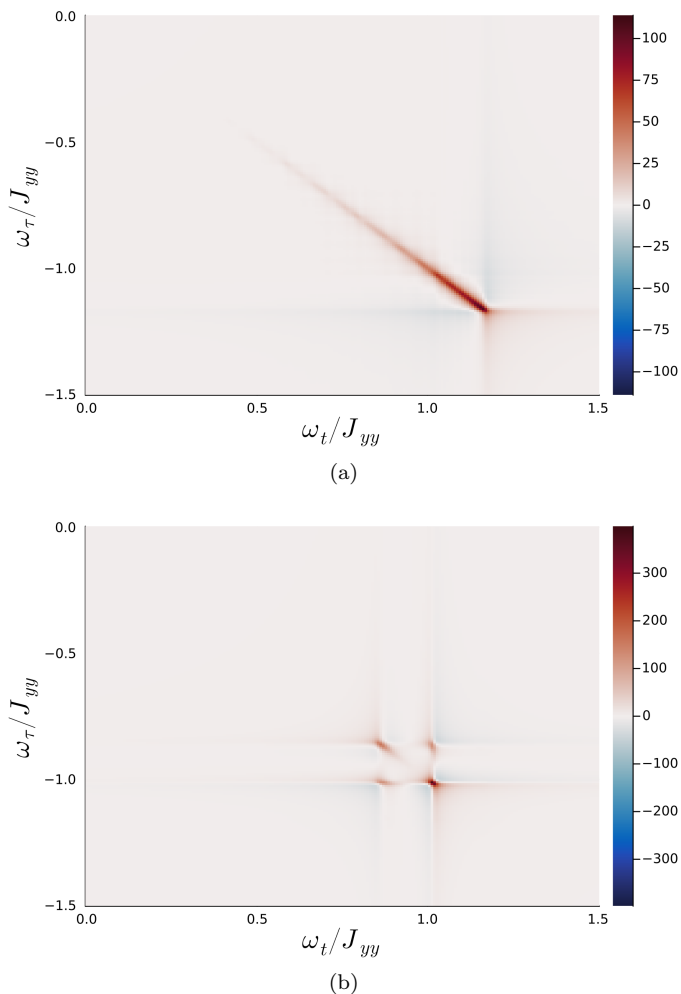


FIG. 3. 2DCS rephasing signals in the low temperature regime from gauge mean field theory. (a) response in the 0-flux phase (with $J_{\pm}/J_{yy} = 0.04$); (b) π -flux response (for $J_{\pm}/J_{yy} = -0.04$). In the 0-flux phase, a single extended streak is observed, whilst in the π -flux phase, the much narrower bandwidth of the two spinon bands, and transitions between them, result in multiple rephasing peaks, and additional peaks away from the main diagonal. Note that, if ϵ_{\pm} are the mean energies of each spinon band, the peaks in the π -flux response occur at frequencies $\omega_i = \epsilon_{-}, (\epsilon_{-} + \epsilon_{+})/2$. Matrix elements for processes where $\omega_i = \epsilon_{+}$ are heavily suppressed. In both cases the Lorentzian linewidth $\Gamma = 0.01$

description of the physics close to $T = 0$.

In this GMFT formulation, a gauge field $A_{i,j}$ and spinon field Φ_i are introduced through the assignment: $S_{i,j}^+ = \Phi_i^\dagger e^{iA_{i,j}} \Phi_j / 2$, where i and j label neighbouring tetrahedra on the ‘A’ and ‘B’ sublattices respectively. The spin component $S_{i,j}^y$ is correspondingly mapped to an emergent electric field $E_{i,j}^y$, which obeys an emergent Gauss’ law. Technical details of the construction used can be found in Ref. [31], where it is also demonstrated that there exist two possible mean field solutions for gapped spinon effective actions consistent with the gauge, time-reversal and lattice symmetries. These are the 0-flux and π -flux

$U(1)$ dipolar-ocutpolar spin ice phases. In both phases, spinons on the ‘A’ and ‘B’ sublattices decouple, and the terms generated by the $J_{\pm\pm}$ term in Eq. (1) vanish in the mean field, again allowing us to freely set the mixing angle θ to zero. In the 0-flux phase, the ‘A’ and ‘B’ sublattice spinons both have a single dispersive band, whilst in the π -flux phase, the threading of π -flux through each hexagonal plaquette of the pyrochlore lattice leads to an enlargement of the unit cell, resulting in two doubly degenerate bands per sublattice.

The two-band dispersion of spinons in the π -flux phase has already been identified as a key signature distinguishing it from the 0-flux regime in linear response [29, 37], and we find that spinon transitions between these two bands produce features in the 2DCS response that clearly distinguish the two phases. Figure 3 presents the 2DCS responses for both phases calculated analytically using GMFT. For the 0-flux phase, a single rephasing streak is obtained, whilst the π -flux response resembles a cluster of isolated peaks. The reason for this stark contrast is two-fold. First, each of the two distinct spinon bands in the π -flux phase are relatively flat, leading to a density of states with two well defined maxima, and hence relatively narrow bandwidth optical responses. Second, the probe operator has non-zero matrix elements to excite a spinon from one band to another, and these inter-band transitions result in the additional peaks off of the main rephasing diagonal. Details of this calculation are given in the supplementary material[35].

Discussion- The 2DCS responses of spinons in dipolar-octupolar QSI are found to be sensitive to both temperature regime and phase of the system. Sharp responses reflecting the presence of fractionalized spinon excitations are predicted for the lowest T , and these responses are demonstrated to clearly distinguish between the spinon dynamics found in the 0-flux and π -flux phases of dipolar-octupolar spin ice. Conversely, in the intermediate temperature regime, a broad non-linear response is observed indicative of heavily constrained spinon motion in the presence of an incoherent spin background.

Whilst this letter has focused on the example of dipolar-octupolar pyrochlores, we hypothesise that the appearance of broad signatures in 2DCS where fractionalised excitations move across an incoherent spin background may occur more generally in similar frustrated models, presenting an obstacle to observing sharp signatures of fractionalisation at all but the lowest temperatures. On the other hand, by measuring the 2DCS signal as a function of temperature one could use the crossover between these regimes to demonstrate the onset of a quantum coherent low-temperature state. The GMFT calculation however does not include the effects of quantum fluctuations in the gauge field, which will be necessary to understand the cross-over between these two regimes.

A natural question is then whether the clear distinctions between the different spinon dynamical regimes observable in 2DCS can be observed more directly in the linear optical response to a uniform magnetic field, which is

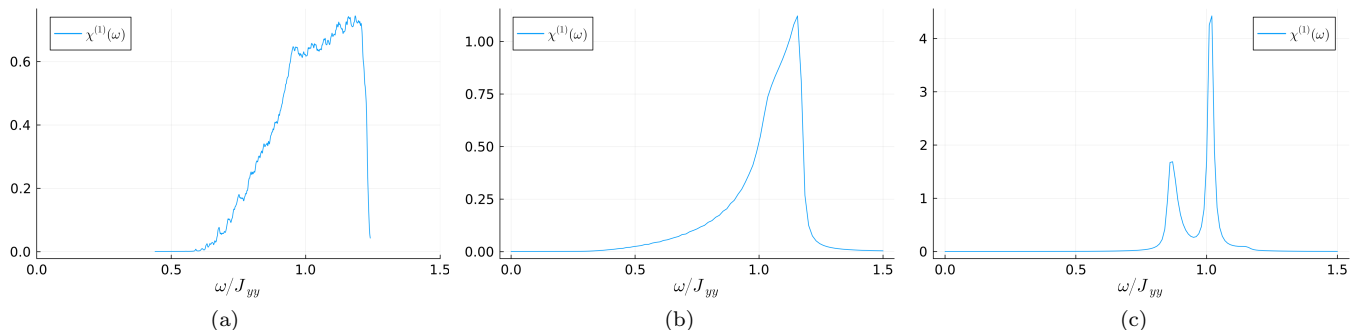


FIG. 4. Linear optical response functions for the intermediate temperature regime ((a)), 0-flux ground state ((b)), and π -flux ground state ((c)). For the intermediate temperature regime and 0-flux response functions, $J_{\pm}/J_{yy} = 0.04$, and for the π -flux $J_{\pm}/J_{yy} = -0.04$. The two ground state phases remain distinguishable in the linear optical response, with the π -flux response possessing multiple clear maxima. However, the qualitatively different behaviour of the 2DCS signal in the intermediate temperature regime to the low energy regime is not evident at linear response, and there is little qualitative difference between the 0-flux response and the response from spinons moving on an incoherent spin background, despite the stark differences in the underlying dynamics. For panel (a), the Lorentzian linewidth $\Gamma = 0.002$, and in panels (b) and (c) $\Gamma = 0.01$.

more simply accessed experimentally. In Fig. 4 we present the linear responses for all phases and regimes considered above. The linear response varies between each regime, and in particular the existence of multiple maxima in the π -flux response distinguishes it from the $T = 0$ 0-flux response, as already noted in Ref. [31]. However, the stark difference between the behaviour of the response in the intermediate temperature regime and the low temperature regime is entirely absent; the intermediate temperature response and the low temperature 0-flux response are not qualitatively different, despite very different underlying spinon dynamics. By contrast, the existence of broad features in the intermediate temperature 2DCS response clearly distinguishes this regime from the low-temperature regime.

To summarise, we find that two-dimensional coherent spectroscopy is a suitable experimental setting to probe the dynamics of fractionalised excitations in candidate quantum spin ice materials, providing clear signatures distinguishing the regime where fractionalised quasiparticles

move ballistically on the pyrochlore lattice at the lowest temperatures from that where their motion is heavily constrained by an incoherent spin background. Further, the appearance of response streaks away from the main rephasing diagonal in 2DCS offers a direct signature of the transition of quasiparticles between bands, which for dipolar-octupolar quantum spin ices allows one to distinguish experimentally between a 0-flux or π -flux QSI ground states. We believe that this further demonstrates the potential utility of 2DCS as a probe of the dynamics of fractionalised excitations in quantum spin ice candidate materials, and other systems potentially hosting exotic quantum phases of matter.

ACKNOWLEDGEMENTS

We thank Benedikt Placke and Yuan Wan for useful discussions. This work was supported in part by the Deutsche Forschungsgemeinschaft under Grant No. SFB 1143 (Project-ID No. 247310070) and by the Deutsche Forschungsgemeinschaft under cluster of excellence ct.qmat (EXC 2147, Project-ID No. 390858490).

-
- [1] R. Rajaraman, “Fractional charge,” (2001), [arXiv:cond-mat/0103366](https://arxiv.org/abs/cond-mat/0103366) [[cond-mat.mes-hall](https://arxiv.org/abs/cond-mat/0103366)].
 - [2] R. Moessner and J. E. Moore, *Topological Phases of Matter* (Cambridge University Press, 2021).
 - [3] P. Anderson, *Materials Research Bulletin* **8**, 153 (1973).
 - [4] R. Moessner and S. L. Sondhi, *Physical Review Letters* **86**, 1881–1884 (2001).
 - [5] L. Balents, *Nature* **464**, 199–208 (2010).
 - [6] J. Knolle and R. Moessner, *Annual Review of Condensed Matter Physics* **10**, 451 (2019), <https://doi.org/10.1146/annurev-conmatphys-031218-013401>.
 - [7] R. B. Laughlin, *Phys. Rev. Lett.* **50**, 1395 (1983).
 - [8] X.-G. Wen, *Phys. Rev. B* **65**, 165113 (2002).
 - [9] Y. Wan and N. P. Armitage, *Phys. Rev. Lett.* **122**, 257401 (2019).
 - [10] W. Kuehn, K. Reimann, M. Woerner, T. Elsaesser, and R. Hey, *The Journal of Physical Chemistry B* **115**, 5448 (2011), pMID: 21171588, <https://doi.org/10.1021/jp1099046>.
 - [11] M. Woerner, W. Kuehn, P. Bownan, K. Reimann, and T. Elsaesser, *New Journal of Physics* **15**, 025039 (2013).
 - [12] W. Choi, K. H. Lee, and Y. B. Kim, *Phys. Rev. Lett.* **124**, 117205 (2020).
 - [13] O. Hart and R. Nandkishore, *Phys. Rev. B* **107**, 205143 (2023).

- [14] Y. Qiang, V. L. Quito, T. V. Trevisan, and P. P. Orth, [arXiv:2301.11243](https://arxiv.org/abs/2301.11243).
- [15] M. Hermele, M. P. A. Fisher, and L. Balents, *Phys. Rev. B* **69**, 064404 (2004).
- [16] N. Shannon, O. Sikora, F. Pollmann, K. Penc, and P. Fulde, *Phys. Rev. Lett.* **108**, 067204 (2012).
- [17] O. Benton, O. Sikora, and N. Shannon, *Phys. Rev. B* **86**, 075154 (2012).
- [18] L. Savary and L. Balents, *Phys. Rev. Lett.* **108**, 037202 (2012).
- [19] M. J. P. Gingras and P. A. McClarty, *Reports on Progress in Physics* **77**, 056501 (2014).
- [20] K. Kimura, S. Nakatsuji, J.-J. Wen, C. Broholm, M. B. Stone, E. Nishibori, and H. Sawa, *Nature Commun.* **4**, 1934 (2013).
- [21] R. Sibille, N. Gauthier, H. Yan, M. Ciomaga Hatnean, J. Olliver, B. Winn, U. Filges, G. Balakrishnan, M. Kenzelmann, N. Shannon, and T. Fennell, *Nat. Phys.* **14**, 711 (2018).
- [22] J. Gaudet, E. M. Smith, J. Dudemaine, J. Beare, C. R. C. Buhariwalla, N. P. Butch, M. B. Stone, A. I. Kolesnikov, G. Xu, D. R. Yahne, K. A. Ross, C. A. Marjerrison, J. D. Garrett, G. M. Luke, A. D. Bianchi, and B. D. Gaulin, *Phys. Rev. Lett.* **122**, 187201 (2019).
- [23] R. Sibille, N. Gauthier, and E. e. a. Lhotel, *Nat. Phys.* **16**, 546 (2020).
- [24] V. Porée, E. Lhotel, S. Petit, A. Krajewska, P. Pupal, A. H. Clark, V. Pomjakushin, H. C. Walker, N. Gauthier, D. J. Gawryluk, and R. Sibille, *Phys. Rev. Mater.* **6**, 044406 (2022).
- [25] V. Porée, A. Bhardwaj, E. Lhotel, S. Petit, N. Gauthier, H. Yan, V. Pomjakushin, J. Ollivier, J. A. Quilliam, A. H. Nevidomskyy, H. J. Changlani, and R. Sibille, “Dipolar-octupolar correlations and hierarchy of exchange interactions in $\text{Ce}_2\text{Hf}_2\text{O}_7$,” (2024), [arXiv:2305.08261](https://arxiv.org/abs/2305.08261) [cond-mat.str-el].
- [26] B. Gao, T. Chen, D. W. Tam, C.-L. Huang, K. Sasmal, D. T. Adroja, F. Ye, H. Cao, G. Sala, M. B. Stone, C. Baines, J. A. T. Verezhak, H. Hu, J.-H. Chung, X. Xu, S.-W. Cheong, M. Nallaiyan, S. Spagna, M. B. Maple, A. H. Nevidomskyy, E. Morosan, G. Chen, and P. Dai, *Nature Physics* **15**, 1052 (2019).
- [27] E. M. Smith, J. Dudemaine, B. Placke, R. Schäfer, D. R. Yahne, T. DeLazzer, A. Fitterman, J. Beare, J. Gaudet, C. R. C. Buhariwalla, A. Podlesnyak, G. Xu, J. P. Clancy, R. Movshovich, G. M. Luke, K. A. Ross, R. Moessner, O. Benton, A. D. Bianchi, and B. D. Gaulin, *Phys. Rev. B* **108**, 054438 (2023).
- [28] D. R. Yahne, B. Placke, R. Schäfer, O. Benton, R. Moessner, M. Powell, J. W. Kolis, C. M. Pasco, A. F. May, M. D. Frontzek, E. M. Smith, B. D. Gaulin, S. Calder, and K. A. Ross, *Phys. Rev. X* **14**, 011005 (2024).
- [29] S. Lee, S. Onoda, and L. Balents, *Phys. Rev. B* **86**, 104412 (2012).
- [30] F. Desrochers, L. E. Chern, and Y. B. Kim, *Phys. Rev. B* **107**, 064404 (2023).
- [31] F. Desrochers and Y. B. Kim, *Phys. Rev. Lett.* **132**, 066502 (2024).
- [32] J. G. Rau and M. J. Gingras, *Annual Review of Condensed Matter Physics* **10**, 357 (2019), <https://doi.org/10.1146/annurev-conmatphys-022317-110520>.
- [33] E. M. Smith, O. Benton, D. R. Yahne, B. Placke, R. Schäfer, J. Gaudet, J. Dudemaine, A. Fitterman, J. Beare, A. R. Wildes, S. Bhattacharya, T. DeLazzer, C. R. C. Buhariwalla, N. P. Butch, R. Movshovich, J. D. Garrett, C. A. Marjerrison, J. P. Clancy, E. Kermarrec, G. M. Luke, A. D. Bianchi, K. A. Ross, and B. D. Gaulin, *Phys. Rev. X* **12**, 021015 (2022).
- [34] Y.-P. Huang, G. Chen, and M. Hermele, *Phys. Rev. Lett.* **112**, 167203 (2014).
- [35] See Supplemental Material at URL-will-be-inserted-by-publisher.
- [36] M. Udagawa and R. Moessner, *Phys. Rev. Lett.* **122**, 117201 (2019).
- [37] F. Desrochers and Y. B. Kim, “Finite temperature dynamics in 0-flux and π -flux quantum spin ice: Self-consistent exclusive boson approach,” (2024), [arXiv:2401.09551](https://arxiv.org/abs/2401.09551) [cond-mat.str-el].

Supplementary material for
'Signatures of spinon dynamics and phase structure of dipolar-octupolar
quantum spin ices in two-dimensional coherent spectroscopy'

arXiv:2406.01472v1 [cond-mat.str-el] 3 Jun 2024

I. PERTURBATION THEORY AND EXACT DIAGONALIZATION FOR INTERMEDIATE TEMPERATURE REGIME

In this section we discuss the treatment of spinon dynamics in the intermediate temperature regime, wherein first order degenerate perturbation theory can be applied. The perturbation Hamiltonian generating spinon dynamics in this limit is given by:

$$H_{\text{eff}} = -J_{\pm} \sum_{\langle i,j \rangle} S_i^+ S_j^- + S_i^- S_j^+. \quad (\text{S1})$$

At first order in perturbation theory this Hamiltonian acts only in a space of states with fixed spinon number. The perturbation can move spinons between tetrahedra on the same fcc sublattice; applying the Hamiltonian to a state with a spinon on a ‘A’ sublattice tetrahedron, gives a superposition of each state where that spinon is on a neighbouring ‘A’ tetrahedron provided that the spinon flips two intermediate spins of opposite initial orientation. For an isolated spinon, six of the twelve neighbouring tetrahedra on the same sublattice are always accessible, but which tetrahedra these are depends on the configuration of surrounding spins.

If two spinons neighbour one another, they can obstruct each other’s motion if they are ‘contractible pairs’ [1]. This refers to two spinons on neighbouring tetrahedra connected by a majority spin (i.e the pair can be annihilated by flipping this spin). Further, the motion of one spinon flips spins in its wake, which then changes the possible sites the other spinon can hop to. The perturbation theory is treated exactly without removing these interaction effects by diagonalising Eq. (S1) on the finite cluster of 32 spins shown in Fig. S1 in the relevant spinon sectors.

To calculate the desired non-linear susceptibility, we expand $\chi^{(3)}$ in the Lehmann representation as follows:

$$\chi^{(3)}(t, t, t + \tau) = \frac{2\theta(t)\theta(\tau)}{N_s} \sum_{p,q,r,m} \langle \emptyset_m | M | E_p \rangle \langle E_p | M | E_q \rangle \langle E_q | M | E_r \rangle \langle E_r | M | \emptyset_m \rangle \text{Im}(G(\{E_i\}, t, \tau)). \quad (\text{S2})$$

Here N_s is the total number of spins (equal to four times the number of ‘A’ tetrahedra which we denote N), and M is the time independent probe field operator $\sum_i (\mathbf{H} \cdot \mathbf{z}_i) S_i^z$ (we have set the parameter θ to zero by exploiting the symmetry of the perturbation Hamiltonian). The temperature is assumed to be sufficiently high that the equilibrium state is an equal weight ensemble of classical ground states, which are indexed with m . The function $G(\{E_i\}, t, \tau)$ contains all time dependent factors, and is given by:

$$G = e^{-iE_p t} e^{-iE_r \tau} + e^{iE_q t} e^{-iE_r(t+\tau)} + 2e^{iE_p \tau} e^{iE_q t} e^{-iE_r t}. \quad (\text{S3})$$

Note that we have set the energy of the ground states E_{\emptyset} to zero.

Acting on a ground state with M creates spinon pairs, with one spinon on the ‘A’ sublattice, and one on the ‘B’ sublattice. At linear response, this is the only subspace over which Eq. (S1) must be diagonalised. This sector has two distinct spaces not connected by the dynamics of the effective Hamiltonian, corresponding to either having a positive spinon (excitation with positive divergence of S^y) on the ‘A’ sublattice and a negative spinon on the ‘B’ sublattice, or vice versa. We name these spaces $\mathcal{H}_{A;B}$ and $\mathcal{H}_{B;A}$ respectively. States in $\mathcal{H}_{B;A}$ can be mapped exactly to states in $\mathcal{H}_{A;B}$ by flipping all spins (an operation we denote I_S). By making use of this relationship, it is only necessary to diagonalize the Hamiltonian in one of these two sectors explicitly.

For non-linear processes, further spinon sectors must be considered. Starting from a state in $\mathcal{H}_{A;B}$, acting with another M operator results either in a state back in the set of ground states \mathcal{H}_{\emptyset} , a state with two spinons on the ‘A’ sublattice ($\mathcal{H}_{A;A}$), a state with two spinons on the ‘B’ sublattice ($\mathcal{H}_{B;B}$), or a state with four spinons. This four spinon state can either have two positive spinons on the ‘A’ sublattice, and two negative spinons on the ‘B’ sublattice ($\mathcal{H}_{AA;BB}$), or it can have spinons of each sign on both sublattices ($\mathcal{H}_{AB;AB}$). Spatial inversion I is a symmetry of the Hamiltonian, and interchanges the sublattices ‘A’ and ‘B’. This symmetry can be used to relate the spaces $\mathcal{H}_{A;A}$ and $\mathcal{H}_{B;B}$, leaving only $\mathcal{H}_{A;B}$, $\mathcal{H}_{A;A}$, $\mathcal{H}_{AA;BB}$, and $\mathcal{H}_{AB;AB}$ as distinct spaces to be diagonalised.

The spinon dynamics generated by the effective Hamiltonian are ergodic within these sectors [1], and so these Hilbert spaces can be generated by taking some initial state in the space and acting iteratively with Eq. (S1) until no new states are found. The resulting Hilbert space dimensions are: $\mathcal{H}_{A;B}$ - 98,784; $\mathcal{H}_{A;A}$ - 82,944; $\mathcal{H}_{AA;BB}$ - 861,584; $\mathcal{H}_{AB;AB}$ - 2,260,352.

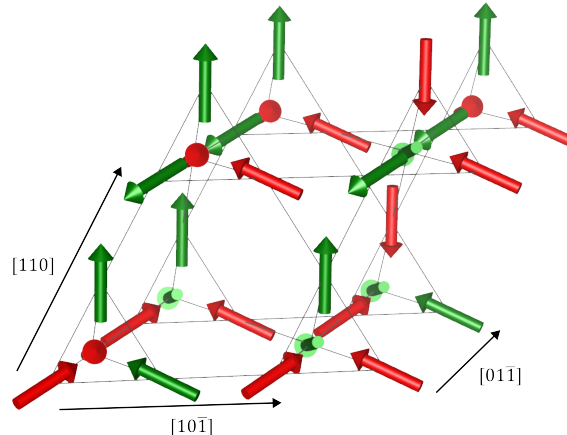


FIG. S1. The 32 site finite cluster of the pyrochlore lattice used for exact diagonalization calculations. Periodic boundary conditions are assumed, such that the cluster possesses 8 ‘A’ tetrahedra and 8 ‘B’ tetrahedra. The spin configuration shown is a ground state, with the ‘2-in-2-out’ rule satisfied on each tetrahedron.

The two-spinon spaces are sufficiently small that we can fully diagonalise them only making use of translational symmetries. For the four-spinon spaces, larger non-abelian symmetry groups were used to reduce the size of these Hilbert spaces [2]. For $\mathcal{H}_{AA;BB}$, the symmetry group used is the octahedral group O_h augmented with the additional generator $I \circ I_S$, whilst $\mathcal{H}_{AB;AB}$ can be reduced using the octahedral group enlarged with the individual generators I and I_S . Both I and I_S commute with all elements of O_h .

With the effective Hamiltonian diagonalised in the relevant spinon sectors, the matrix elements in the Lehmann representation of Eq. (S2) can be calculated explicitly. One remaining numerical issue is the large number of such matrix elements that must be summed together for each value of ω_t and ω_τ in the desired section of the two dimensional frequency plane. Taking the Fourier transform of the time dependent factors in Eq. (S2), and introducing a regulating factor Γ , one finds that the 2DCS response is a weighted sum of peak functions of the general functional form:

$$\frac{\Gamma}{\Gamma^2 + \omega_t^2} \frac{\Gamma}{\Gamma^2 + \omega_\tau^2} - \frac{\omega_t}{\Gamma^2 + \omega_t^2} \frac{\omega_\tau}{\Gamma^2 + \omega_\tau^2}. \quad (\text{S4})$$

This function is largest when $|\omega_t|, |\omega_\tau| < \Gamma$, and we make the approximation of cutting off each peak function beyond this limit, which limits the number of matrix elements that need to be included for each ω_t, ω_τ , and greatly improves computational performance. In doing this, we are cutting off the ‘tails’ of the $1/x$ like parts of the peak functions, however the most important feature of the second term - the variation in sign about the centre of the peak- is retained. This sign structure is responsible for washing out a signature similar to the rephasing signal along the $\omega_t = \omega_\tau$ axis which is present if only the delta function or Lorentzian part of the peak function is kept [3]. ‘Phase untwisting’ procedures [4] can be used in certain circumstances to restore this signal, but generically only the rephasing signal along the $\omega_t = -\omega_\tau$ line is robust to the sign variations introduced in the second term of Eq. S4.

II. HUSIMI CACTUS MODEL OF SPINON DYNAMICS IN THE INTERMEDIATE TEMPERATURE REGIME

In this section, we detail an approximate analytic treatment of the perturbation Hamiltonian S1 in the intermediate temperature limit through which a qualitative understanding of our key result - the appearance of broad features in the 2DCS response in this regime - can be gained.

Following the assumptions made in the main text, we define an effective Hamiltonian describing the dynamics of a single spinon as:

$$H_{\text{eff}} = -J_{\pm} \sum_{\langle i,j \rangle} |i\rangle \langle j| + |i\rangle \langle j|, \quad (\text{S5})$$

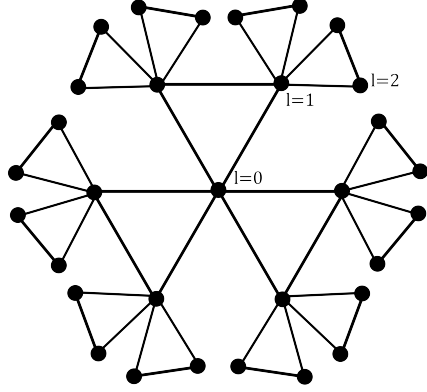


FIG. S2. Diagram of the Husimi cactus for a single spinon. Each vertex represents a many-body state of the system, and each edge links states connected by the hopping of a single spinon under the dynamics of the first order perturbation Hamiltonian of Eq. (S5). The graph is self similar, and continues infinitely beyond what is shown. Points on the graph are labelled with a layer index l with respect to an arbitrarily chosen origin.

where the states $|i\rangle$ correspond to points on the Husimi cactus graph replicated in Fig. S2, and $\langle i, j \rangle$ enumerates all pairs of points connected by edges [1]. Each of these states $|i\rangle$ approximately correspond to a particular spin configuration on the pyrochlore lattice, and the edges connect states linked by the hopping of a single spinon. If we were treating the degenerate perturbation theory exactly, interaction effects between spinons and the effects of the Dirac string between them prevent a decomposition of the many-body state graph into two single body graphs. Thus in constructing a graph where only single spinon motion is considered, we are ignoring these interactions, which one expects to not be too great an approximation provided the equilibrium density of spinons vanishes.

Further, as described in the main text, all loops of size greater than three are ignored, resulting in the Bethe lattice-like form of the approximate many-body state graph. Making these approximations, there is no longer any exact mapping between real spin configurations and states on the Husimi cactus, but the Husimi states can still be qualitatively understood as corresponding to different spinon locations and surrounding spin backgrounds.

It is possible to obtain the single spinon density of states using Green's functions methods [1], however here we present a formulation of the single spinon dynamics in terms of explicit eigenstates of S5. The simplest ansatz we might try in attempting to construct an eigenstate is a form with only radial dependence about a chosen point on the lattice. Indexing 'layers' of the Husimi cactus away from the chosen origin with l as shown in Fig. S2, wavefunctions of this form must satisfy:

$$\lambda\psi_l = 4\psi_{l+1} + \psi_l + \psi_{l-1}; \quad l \geq 1, \quad (\text{S6})$$

$$\lambda\psi_0 = 6\psi_1. \quad (\text{S7})$$

These equations are satisfied by the following wavefunction:

$$\psi_l = \sqrt{\frac{4}{3}} \frac{1}{2^l} \cos(pl + \varphi_p), \quad (\text{S8})$$

with

$$\tan \varphi_p = -\frac{1}{3} \cot\left(\frac{p}{2}\right), \quad (\text{S9})$$

and energy eigenvalue:

$$\lambda_p = -J_{\pm}(4 \cos(p) + 1). \quad (\text{S10})$$

These 'ripple' eigenstates are defined for $0 < p \leq \pi$, where p is a one-dimensional pseudo-momentum. In bra-ket notation, we represent a ripple state with pseudo-momentum p with state $|i\rangle$ taken as the origin as $|p; i\rangle$. These states are normalised such that $\langle p; i | q; i \rangle = \pi \delta(p - q)$.

One can demonstrate that such ripple states, centred about each state $|i\rangle$ on the Husimi cactus, are a sufficient basis to describe every eigenstate of the graph, and hence Eq. (S10) describes the full spectrum of a single spinon. To see this, we can define a projector P_i that projects onto the set of all ripple states about $|i\rangle$. If we then take this projector and act with it upon $|i\rangle$, we find:

$$P_i |i\rangle = \int_0^\pi \frac{dp}{\pi} |p; i\rangle \langle p; i|i\rangle = \int_0^\pi \frac{dp}{\pi} \frac{4}{3} |p; i\rangle \cos(\varphi_p). \quad (\text{S11})$$

Taking the inner product with the original state $|i\rangle$, we obtain:

$$\langle i|P_i|i\rangle = \int_0^\pi \frac{dp}{\pi} \frac{4}{3} \cos^2(\varphi_p) = 1, \quad (\text{S12})$$

therefore the projector acts as the identity on $|i\rangle$, meaning that each ‘position’ eigenstate on the Husimi cactus can be exactly decomposed into ripple states, and thus these states span the full Hilbert space.

Armed with this ripple state expansion, we can calculate the ‘local’ single spinon density of states (local here with respect to states of the Husimi cactus, which roughly correspond to localised spinon states on the pyrochlore lattice). This is found to be:

$$\rho^{(1)}(\epsilon) = \int_0^\pi \frac{dp}{\pi} \frac{4}{3} \cos^2(\varphi_p) \delta(\epsilon - \lambda_p), \quad (\text{S13})$$

$$= \frac{4}{3\pi} \frac{\cos^2\left(\arctan\left(\frac{1}{3} \cot\left(\frac{\arccos\left(\frac{\epsilon-1}{4}\right)}{2}\right)\right)\right)}{\sqrt{(5-\epsilon)(3+\epsilon)}}, \quad (\text{S14})$$

$$= \frac{3}{2\pi} \frac{1}{6-\epsilon} \sqrt{\frac{5-\epsilon}{3+\epsilon}}, \quad (\text{S15})$$

which is precisely the function obtained in Ref. [1] through Green’s functions methods, corroborating that the ripple state functions are sufficient to capture the full dynamics on the Husimi cactus.

In order to calculate response functions in this language, we need a way to stitch together the two different spinon sublattices of the pyrochlore lattice. A single spinon moves on just one of these sublattices, but the operator S^z we use to probe the system will move spinons from one sublattice to the other, or create pairs of spinons on opposite sublattices. The current Husimi construction must be extended to account for this physics.

Each spinon sits on a tetrahedron with three spins of a certain orientation (majority spin), and one of the other (minority spin). If a spinon hops onto the opposite sublattice, it can only do so by flipping a majority spin, as flipping the minority spin will just create an additional pair of spinons. Thus each spinon state, and hence each state $|i\rangle$ on the Husimi cactus, can be connected to three states with a spinon on the opposite sublattice by S^z . In the spirit of previous approximations, we will keep this local structure, whilst discarding any longer range connections between the two networks of states, giving us the dual Husimi cactus graph presented in Fig. S3. The black and green networks correspond to many-body states with single spinons on the ‘A’ and ‘B’ sublattices respectively, whilst the blue dotted lines correspond to the majority spins flipped by S^z to move the spinon from one to the other.

Using this picture, we can now calculate the linear response of the system to a magnetic probe field. We will consider two different probe field configurations, the first being a field that conserves the spinon pseudo-momentum: $M_1(t) = \sum_{\tilde{i}} S_{\tilde{i}}^z$, and the second a more realistic field which is uniform in physical space: $M_2(t) = \sum_{\tilde{i}} (\mathbf{h} \cdot \mathbf{z}_{\tilde{i}}) S_{\tilde{i}}^z$. Here $\mathbf{h} = \mathbf{H}/|\mathbf{H}|$, and roman indices with tildes refer to tetrahedra on the pyrochlore lattice proper, and not to Husimi states. Using the Lehmann representation, the linear response in the case of a pseudo-momentum conserving probe is given on the real lattice by:

$$\chi^{(1)}(t) = \frac{\theta(t)}{2N} \sum_{\tilde{j}, \tilde{l}} \sum_{m,p} \frac{1}{N_{\text{GS}}} \langle \emptyset_m | \sigma_{\tilde{j}}^z | E_p \rangle \langle E_p | \sigma_{\tilde{l}}^z | \emptyset_m \rangle \sin(E_p t). \quad (\text{S16})$$

Mapping to the dual Husimi cacti, we find that as we no longer have any loops of size greater than three, there are no processes by which spinons can be created, evolve in time, and be destroyed such that one returns to a different ground state. In the Husimi picture, each ground state is identical, and has no

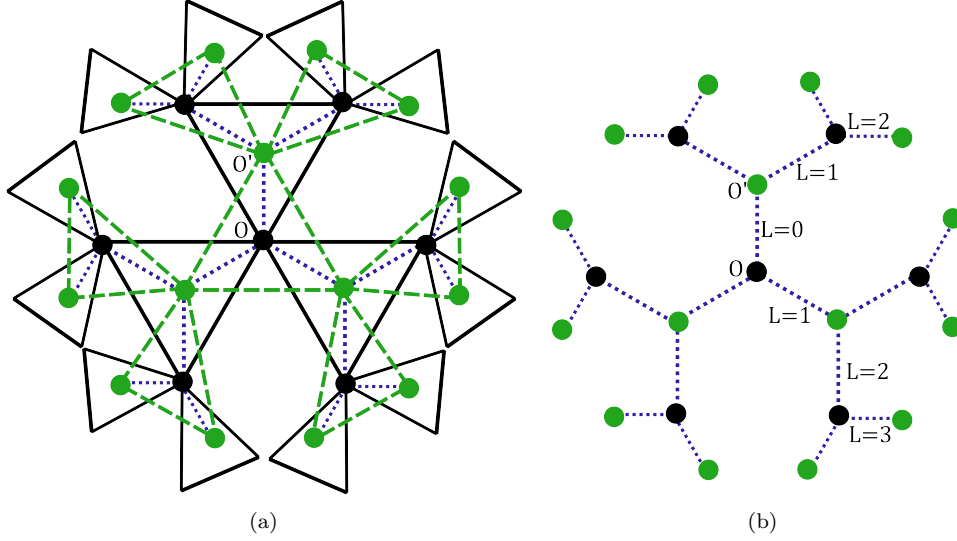


FIG. S3. Panel (a) is a diagram of the dual Husimi cacti, with the black network representing the ‘A’ sublattice, and the green dashed network the ‘B’ sublattice. These networks are connected by dotted blue lines which represent the majority spins of a tetrahedron hosting a spinon that can be flipped to move it from one sublattice to the other. Panel (b) shows just the network of these majority spin ‘bonds’, with labels indicating the bond layer with respect to the bond connecting the two origins of the dual cacti, O and O' .

influence on the spinon dynamics, and so we are able to evaluate the sum over ground states trivially. The states $|\emptyset_m\rangle$ are thus replaced with a representative state $|\emptyset\rangle$. For the sums over pyrochlore lattice spins we substitute a sum over the Husimi bonds between the two dual Husimi cacti in Fig. S3. The action of each σ_i^z is then to create/destroy a spinon if it is located on either of the Husimi sites connected to that bond, which replicates the effects of flipping a spin on the real lattice. The eigenstates $|E_p\rangle$ at linear response are two-spinon eigenstates, which in this the non-interacting picture are tensor products of spinon eigenstates on either sublattice graph. The linear response becomes:

$$\chi^{(1)}(t) = \frac{\theta(t)}{2N} \sum_{\vec{j}, \vec{l}} \sum_{p, q} \langle \emptyset | \sigma_j^z | E_{p_1} \rangle \langle E_{p_1} | \otimes | E_{p_2} \rangle \langle E_{p_2} | \sigma_l^z | \emptyset \rangle \sin((E_{p_1} + E_{p_2})t). \quad (\text{S17})$$

Using the translational symmetry of the dual Husimi graphs, we can keep the bond j fixed, labelling the neighbouring Husimi sites as O and O' (see Fig. S3) which act as origins for the dual graphs. Acting on the spinon vacuum, σ_O^z creates two spinons, one at O on the ‘A’ cactus, and one at O' on the ‘B’ cactus. Using the property that the ripple state projector centred on any given Husimi state acts as the identity on that state, we can expand $\sigma_O^z |\emptyset\rangle$ in terms of ripple states on each sublattice, and thus set $|E_{p_1}\rangle = |p_1; O\rangle$ and $|E_{p_2}\rangle = |p_2; O'\rangle$, giving:

$$\chi^{(1)}(t) = \frac{\theta(t)}{2} \sum_l \sum_{p_i} \langle O | p_1; O \rangle \langle O' | p_2; O' \rangle \langle p_1; O | A_l \rangle \langle p_2; O' | B_l \rangle \sin((E_{p_1} + E_{p_2})t). \quad (\text{S18})$$

We have also acted with σ_l^z on $|\emptyset\rangle$, which produces a spinon on each site at either end of the bond l . The vertex connected to l on the ‘A’ sublattice we denote A_l , and that on the ‘B’ sublattice is denoted B_l . Now, using $\langle O | p_i; O \rangle = \sqrt{\frac{4}{3}} \cos(\varphi_{p_i})$ we have:

$$\sum_l \langle p_1; O | A_l \rangle \langle p_2; O' | B_l \rangle = \sum_l \frac{4}{3} \frac{1}{2^{L(A_l)+L'(B_l)}} \cos(p_1 L(A_l) + \varphi_{p_1}) \cos(p_2 L'(B_l) + \varphi_{p_2}), \quad (\text{S19})$$

where $L(A_l)$ is the layer index of A_l with respect to the origin of the ‘A’ graph O , and $L'(B_l)$ is the index

of B_l with respect to the ‘B’ origin O' . This sum can be organised into the following form:

$$\begin{aligned} \sum_l \langle p_1; O|A_l \rangle \langle p_2; O'|B_l \rangle &= \lim_{\mathcal{L} \rightarrow \infty} \frac{4}{3} \left\{ \cos(\varphi_{p_1}) \left[\cos \varphi_{p_2} + 2 \cdot \frac{1}{2} \cos(p_2 + \varphi_{p_2}) \right] \right. \\ &+ 2 \sum_{L=1}^{\mathcal{L}} 4^{L-1} \frac{1}{2^L} \cos(p_1 L + \varphi_{p_1}) \left[\frac{1}{2^{L-1}} \cos(p_2(L-1) + \varphi_{p_2}) + \frac{2}{2^L} \cos(p_2 L + \varphi_{p_2}) \right] \\ &\left. + 4 \sum_{L=1}^{\mathcal{L}} 4^{L-1} \frac{1}{2^L} \cos(p_1 L + \varphi_{p_1}) \left[\frac{1}{2^L} \cos(p_2 L + \varphi_{p_2}) + \frac{2}{2^{L+1}} \cos(p_2(L+1) + \varphi_{p_2}) \right] \right\}. \quad (\text{S20}) \end{aligned}$$

Rearranging this by grouping terms, we get:

$$\lim_{\mathcal{L} \rightarrow \infty} \frac{4}{3} \left\{ \cos(\varphi_{p_1}) [\cos \varphi_{p_2} + \cos(p_2 + \varphi_{p_2})] + \sum_{L=1}^{\mathcal{L}} \cos(p_1 L + \varphi_{p_1}) \cos(p_2 L + \varphi_{p_2}) [2 + 2 \cos(p_2)] \right\}. \quad (\text{S21})$$

The infinite series of partial sums found by evaluating the sequence in Eq. (S21) is in general oscillatory, but diverges when $p_1 = p_2$, and can be evaluated to $\frac{\pi}{2} \delta(0)$. The oscillatory parts average to zero, and so we keep only this divergent part leaving us with the desired result of:

$$\sum_l \langle p_1; O|A_l \rangle \langle p_2; O'|B_l \rangle = \frac{4}{3} (1 + \cos(p_1)) \pi \delta(p_1 - p_2). \quad (\text{S22})$$

Plugging this back into the expression for $\chi^{(1)}(t)$, we find in full that:

$$\chi^{(1)}(t) = \frac{\theta(t)}{2} \int_0^\pi \frac{dp}{\pi} \left(\frac{4}{3} \right)^2 \cos(\varphi_p)^2 (1 + \cos(p)) \sin(2\lambda_p t). \quad (\text{S23})$$

The single spinon density of states in momentum is proportional to $\cos(\varphi_p)^2$, and we see that the linear response kernel is simply this single particle density of states weighted by an additional factor of $(1 + \cos(p))$. This factor is essentially a structure factor which accounts for the three possible spins that can be flipped to hop a spinon from a given tetrahedron. This single spinon density of states factor is expected for the response to a uniform zero momentum probe field (as opposed to the two particle density of states found for the momentum integrated response).

We can generalise this calculation to the third order response required to obtain the 2DCS signal. This involves evaluating similar matrix elements as for the linear response, which we will detail briefly below. The end result for the third-order response to the $M_1(t)$ probe is the following:

$$\begin{aligned} \chi_{xxxx}^{(3)}(t_3, t_2 + t_3, t_1 + t_2 + t_3) &= \frac{\theta(t_1)\theta(t_2)\theta(t_3)}{4} \int d\epsilon \rho^{(1)}(\epsilon) F(p(\epsilon)) \\ &\left\{ -2 \sin(2\epsilon(t_1 + t_2 + t_2)) + 2 \sin(2\epsilon(t_1 + t_2)) + \sin(2\epsilon(t_3 + t_1)) + \sin(2\epsilon(t_3 - t_1)) \right\}. \quad (\text{S24}) \end{aligned}$$

The third-order response reduces to a single integral over energy, and the integrand is proportional to the single density particle of states. Crucially the time dependent factors include the term $\sin(2\epsilon(t_3 - t_1))$ which gives rise to the rephasing signal [3], and so we expect a 2DCS rephasing streak which exposes the single-body spinon spectrum as desired.

Evaluating the matrix elements required for the non-linear response produces the function $F(p(\epsilon))$, which is analogous to the factor $\frac{4}{3}(1 + \cos(p))$ encountered in linear response. Again, it is a structure factor accounting for the multiple ways of hopping a spinon onto and off of any given site. The function $F(p)$ is defined such that:

$$F(p_1) \pi \delta(p_1 - p_2) = \frac{4}{3} \cos(\varphi_{p_1}) \cos(\varphi_{p_2}) \sum_l \tilde{f}(p_1; O, B_l) \tilde{f}(p_2; O', A_l), \quad (\text{S25})$$

where $\tilde{f}(p; O, B_l)$ (multiplied by a delta-function) is the amplitude for the probe field $\sum_j \sigma_j^z$ to take a ripple state of pseudo-momentum p centred at O to one of the same pseudo-momentum centred at B_l :

$$\tilde{f}(p_1; O, B_l) \pi \delta(p_1 - p_2) = \sum_j \langle p_1; O|A_j \rangle \langle B_j|p_2; B_l \rangle. \quad (\text{S26})$$

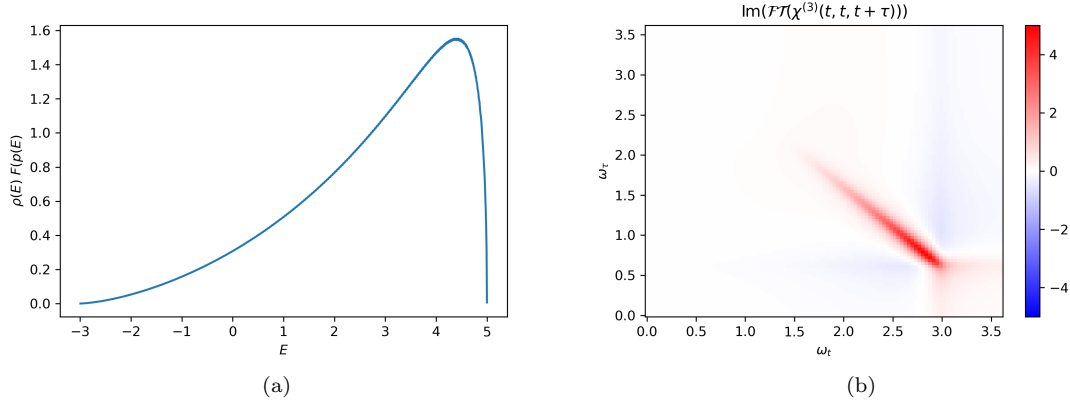


FIG. S4. Panel (a): the function $\rho^{(1)}(E)F(p(E))$ for $J_{\pm} = -1$. The lower end of the spectrum corresponds to high pseudo-momenta. The single particle density of states has a divergence at $p = \pi$, however the function $F(p)$ suppresses this divergence, and leads to a maximum in the 2DCS response towards the low pseudo-momentum part of the spectrum, where the single spinon density of states is lowest. Panel (b) presents the resulting 2DCS response assuming $J_{yy} = 4$ and $J_{\pm} = -0.1$, and a Lorentzian regularization parameter $\Gamma = 0.05$.

Note that $\tilde{f}(p; O, O') = \frac{4}{3}(1 + \cos(p))$ is the linear response structure factor. A numerical evaluation of $\rho^{(1)}F(p)$ is presented in the first panel of Fig. S4. In the second, the 2DCS rephasing signal as calculated using S24 is shown. Just as found using exact diagonalization, a sharp response is obtained, with the greatest spectral weight being at the upper end of the spectrum, where the density of states is small.

This situation is then contrasted with the response to a realistic probe field $M_2(t) = \sum_i (\mathbf{h} \cdot \mathbf{z}_i)$ uniform across the physical pyrochlore lattice. The immediate problem that arises is that the dual Husimi cactus construction necessarily throws away any reference to the geometry of the original lattice. Each of the blue bonds connecting the two Husimi cacti in Fig. S3 represents a majority spin, which is associated with one of the four vectors \mathbf{z}_i ($i = 0, 1, 2, 3$). However, for a given tetrahedron, which of these four spins are the three majority spins when the tetrahedron hosts a spinon excitation depends on the ground state spin configuration.

Fortunately, our initial state is an equal weight ensemble of every classical ground state, and so we can map the action of $M_2(t)$ onto the Husimi cactus by finding the average action of the field across this ensemble. Our strategy is to assign to each spin ‘bond’ in Fig. S3 a random variable ξ_i which have one of four values from $(\mathbf{h} \cdot \mathbf{z}_i)$ for $i = 0, 1, 2, 3$. These variables then reflect the variation in which of the four spins on a given tetrahedron are the three majority spins as the ground state spin configuration is varied with fixed spinon locations. Referring to Fig. S3, sets of three spin ‘bonds’ that meet at ‘A’ (black) or ‘B’ (green) sublattice points correspond to spins on the same tetrahedra, and so must all take different values of $(\mathbf{h} \cdot \mathbf{z}_i)$. If an assignment of ξ_i values satisfies this constraint, it is a valid configuration. As each ground state is equally probable in our initial equilibrium state, so too is each valid assignment of ξ_i .

Using this assignment of random variables and replacing the average over ground states with an average over valid ξ_i configurations, the linear response function to an $M_2(t)$ probe becomes:

$$\chi^{(1)}(t) = \frac{\theta(t)}{2} \sum_l \sum_{p_1, p_2} \langle \xi_O \xi_l \rangle_{\text{GS}} \langle O | p_1; O \rangle \langle O' | p_2; O' \rangle \langle p_1; O | A_l \rangle \langle p_2; O' | B_l \rangle \sin((E_{p_1} + E_{p_2})t), \quad (\text{S27})$$

where $\langle \cdot \rangle_{\text{GS}}$ is equivalently the average over ground states and the average over assignment of ξ_i variables.

We can evaluate $\langle \xi_O \xi_l \rangle_{\text{GS}}$ explicitly as a function of \mathbf{h} as follows. With equal probability, ξ_O , the value assigned to the bond between the points O and O' in Fig. S3, takes one of the four values $(\mathbf{h} \cdot \mathbf{z}_i)$ for $i = 0, 1, 2, 3$. Further ξ_j values are then constrained by the value of this central bond, and we can evaluate the probability P_s that they share the same value of $(\mathbf{h} \cdot \mathbf{z}_i)$ as the central bond, and the probability P_d that they have a different value. By the symmetry of the graph, these probabilities will only vary with the number of other bonds between a given spin bond and the central bond, and so we introduce a new layer index L , defined as shown in the second panel of Fig. S3.

By definition, $P_s^{L=0} = 1$ and $P_d^0 = 0$. Due to the constraint, the ξ_i values on the next layer must be different from that on layer 0, and so we have $P_d^1 = 1$ and $P_s^1 = 0$. In general, if the probability that ξ_i is the same as ξ_O on layer $L-1$ is P_s^{L-1} , then P_s^L is given by the following relation:

$$P_s^L = \frac{1}{3} (1 - P_s^{L-1}). \quad (\text{S28})$$

Solving this recurrence relation with the initial condition $P_s^0 = 1$, one obtains:

$$P_s^L = \frac{1}{4} \left(1 + 3 \left(-\frac{1}{3} \right)^L \right). \quad (\text{S29})$$

Using this, we can evaluate $\langle \xi_O \xi_L \rangle_{\text{GS}}$ by averaging over each of the four values of ξ_O as a function of the bond layer L . We find:

$$\langle \xi_O \xi_L \rangle_{\text{GS}} = \frac{1}{4} \left(P_s^L \sum_{\vec{i}} (\mathbf{h} \cdot \mathbf{z}_{\vec{i}})^2 + \frac{(1 - P_s^L)}{3} \sum_{\vec{i}, \vec{j} \neq \vec{i}} (\mathbf{h} \cdot \mathbf{z}_{\vec{i}}) (\mathbf{h} \cdot \mathbf{z}_{\vec{j}}) \right). \quad (\text{S30})$$

Expanding this, all dependence on the orientation of the probe field is removed, and we are left with:

$$\langle \xi_O \xi_L \rangle_{\text{GS}} = \frac{1}{3} \left(-\frac{1}{3} \right)^L. \quad (\text{S31})$$

When this function is inserted back into the linear response, we find that equivalent of Eq. (S20) which assured conservation of momentum is now:

$$\begin{aligned} \sum_l \langle p_1; O|A_l \rangle \langle p_2; O'|B_l \rangle \langle \xi_O \xi_{L(l)} \rangle_{\text{GS}} &= \lim_{\mathcal{L} \rightarrow \infty} \frac{4}{9} \left\{ \cos \varphi_{p_1} \left[\cos \varphi_{p_2} + \left(-\frac{1}{3} \right) \cos(p_2 + \varphi_{p_2}) \right] \right. \\ &+ 2 \sum_{L=1}^{\mathcal{L}} \frac{4^{L-1}}{2^L} \cos(p_1 L + \varphi_{p_1}) \left[\left(-\frac{1}{3} \right)^{2L-1} \frac{1}{2^{L-1}} \cos(p_2(L-1) + \varphi_{p_2}) + 2 \left(-\frac{1}{3} \right)^{2L} \frac{1}{2^L} \cos(p_2 L + \varphi_{p_2}) \right] \\ &\left. + 4 \sum_{L=1}^{\mathcal{L}} \frac{4^{L-1}}{2^L} \cos(p_1 L + \varphi_{p_1}) \left[\left(-\frac{1}{3} \right)^{2L} \frac{1}{2^L} \cos(p_2 L + \varphi_{p_2}) + 2 \left(-\frac{1}{3} \right)^{2(L+1)} \frac{1}{2^{L+1}} \cos(p_2(L+1) + \varphi_{p_2}) \right] \right\}. \end{aligned} \quad (\text{S32})$$

The infinite sums now converge, and so this is no longer proportional to a delta function in p_1 and p_2 . The $\langle \xi_O \xi_{L(l)} \rangle_{\text{GS}}$ introduced by the geometrical coupling factors are not periodic in L , and so do not conserve the spinon pseudo-momentum. We obtain instead the following function of p_1 and p_2 :

$$\begin{aligned} F(p_1, p_2) &\equiv \frac{4}{9} \left\{ \cos \varphi_{p_1} \left[\cos \varphi_{p_2} + \left(-\frac{1}{3} \right) \cos(p_2 + \varphi_{p_2}) \right] \right. \\ &+ \frac{1}{2} \left(2 - \frac{10}{3} \cos(p_2) \right) \left\{ \frac{9 \cos(p_1 + p_2 + \varphi_{p_1} + \varphi_{p_2}) - \cos(\varphi_{p_1} + \varphi_{p_2})}{82 - 18 \cos(p_1 + p_2)} + \frac{9 \cos(p_1 - p_2 + \varphi_{p_1} - \varphi_{p_2}) - \cos(\varphi_{p_1} - \varphi_{p_2})}{82 - 18 \cos(p_1 - p_2)} \right\} \\ &\left. + \frac{1}{2} \left(-\frac{8}{3} \sin(p_2) \right) \left\{ \frac{9 \sin(p_1 + p_2 + \varphi_{p_1} + \varphi_{p_2}) - \sin(\varphi_{p_1} + \varphi_{p_2})}{82 - 18 \cos(p_1 + p_2)} - \frac{9 \sin(p_1 - p_2 + \varphi_{p_1} - \varphi_{p_2}) - \sin(\varphi_{p_1} - \varphi_{p_2})}{82 - 18 \cos(p_1 - p_2)} \right\} \right\}. \end{aligned} \quad (\text{S33})$$

$F(p_1, p_2)$ is a smooth function of both momenta, and is large where the density of states is large.

Without a delta function enforcing $p_1 = p_2$, we no longer have a linear response kernel proportional to the single body density of states. Further, whilst the constraints on the ξ_i values make the evaluation of higher order correlation functions impractical analytically, correlations between the ξ_i will still generically decay exponentially, and so pseudo-momentum will also fail to be conserved in these higher response functions. Hence, the broad rephasing signal in the 2DCS response for QSI in the intermediate temperature regime presented in the main text.

III. GAUGE MEAN FIELD THEORY NON-LINEAR RESPONSES

We will here expand on some of the details of the GMFT calculation whose results are presented in the main text. Most of the ground work for these calculations can be found in Ref. [5], including an in depth symmetry analysis determining the allowed GMFT ansätze that respect the gauge projective symmetries of the system. We shall forgo repeating that discussion here, and take as our starting point the GMFT effective action for the spinon field Φ in one of the two quantum spin ice phases at finite temperature.

Before writing down this action, we will first introduce the notation of Ref. [5] for ease of comparison. Basis vectors \hat{e}_μ are defined that span each of the ‘A’ and ‘B’ tetrahedron sublattices:

$$\begin{aligned}\hat{e}_1 &= \frac{1}{2}(0, 1, 1), \\ \hat{e}_2 &= \frac{1}{2}(1, 0, 1), \\ \hat{e}_3 &= \frac{1}{2}(1, 1, 0).\end{aligned}\tag{S34}$$

Vectors \mathbf{b}_i are also defined which translate one from a given ‘A’ tetrahedron to one of the four neighbouring ‘B’ tetrahedra:

$$\begin{aligned}\mathbf{b}_0 &= -\frac{1}{4}(1, 1, 1), \\ \mathbf{b}_1 &= \frac{1}{4}(-1, 1, 1), \\ \mathbf{b}_2 &= \frac{1}{2}(1, -1, 1), \\ \mathbf{b}_3 &= \frac{1}{2}(1, 1, -1),\end{aligned}\tag{S35}$$

Note that these are simply re-normalised versions of the \mathbf{z}_i vectors discussed in the main text. One can now index any tetrahedron on the pyrochlore lattice as follows:

$$\mathbf{r}_\alpha = (r_1, r_2, r_3, \alpha) = r_1\hat{e}_1 + r_2\hat{e}_2 + r_3\hat{e}_3 - \frac{\eta_\alpha}{2}\mathbf{b}_0,\tag{S36}$$

where the origin is centred on a spin, and $\eta_A = 1$ and $\eta_B = -1$.

The spinon fields $\Phi_{\mathbf{r}_\alpha}$ are quantum rotors, which generate charge $Q_{\mathbf{r}_\alpha}$. If $\varphi_{\mathbf{r}_\alpha}$ is the conjugate variable to the charge, which can take any integer value, then the spinon field must be equivalent to $e^{i\varphi_{\mathbf{r}_\alpha}}$, and so must satisfy the rotor constraint $|\Phi_{\mathbf{r}_\alpha}^\dagger \Phi_{\mathbf{r}_\alpha}| = 1$. This constraint is enforced through the addition of Lagrange multipliers to the effective spinon action.

The GMFT effective action for the gapped spinon phases of dipolar-octupolar pyrochlores is given by:

$$\begin{aligned}S_{GMFT} &= \int_0^\beta d\tau \sum_{\mathbf{r}_\alpha} \left(\frac{1}{2J_{yy}} \partial_\tau \Phi_{\mathbf{r}_\alpha}^{\tau*} \partial_\tau \Phi_{\mathbf{r}_\alpha}^\tau + \lambda_{\mathbf{r}_\alpha}^\tau (\Phi_{\mathbf{r}_\alpha}^{\tau*} \Phi_{\mathbf{r}_\alpha}^\tau - 1) \right. \\ &\quad \left. - \frac{J_\pm}{4} \sum_{\mu, \nu \neq \mu} \Phi_{\mathbf{r}_\alpha + \eta_\alpha \mathbf{b}_\mu}^{\tau*} \Phi_{\mathbf{r}_\alpha + \eta_\alpha \mathbf{b}_\nu}^\tau e^{i(\bar{A}_{\mathbf{r}_\alpha, \mathbf{r}_\alpha + \eta_\alpha \mathbf{b}_\nu} - \bar{A}_{\mathbf{r}_\alpha, \mathbf{r}_\alpha + \eta_\alpha \mathbf{b}_\mu})} \right).\end{aligned}\tag{S37}$$

Note that the action has no terms coupling the ‘A’ and ‘B’ sublattices. The two possible $U(1)$ symmetric ansätze for the gauge field are the $U(1)_0$ and $U(1)_\pi$ phases. In the $U(1)_0$ phase, the mean gauge field \bar{A} can be set to zero everywhere, whilst in the $U(1)_\pi$ phase, each hexagonal plaquette is threaded with π units of flux. For a particular choice of gauge, this is achieved using the following ansatz for \bar{A} :

$$\begin{aligned}\bar{A}_{(r_1, r_2, r_3)_A, (r_1, r_2, r_3)_B} &= 0, \\ \bar{A}_{(r_1, r_2, r_3)_A, (r_1+1, r_2, r_3)_B} &= \pi(r_2 + r_3), \\ \bar{A}_{(r_1, r_2, r_3)_A, (r_1, r_2+1, r_3)_B} &= \pi r_3, \\ \bar{A}_{(r_1, r_2, r_3)_A, (r_1, r_2, r_3+1)_B} &= 0.\end{aligned}\tag{S38}$$

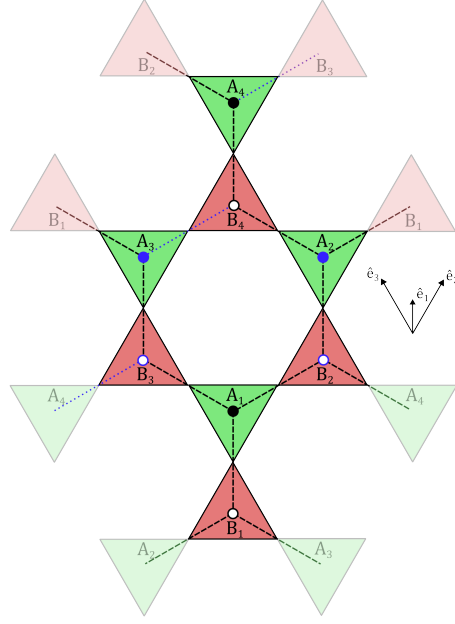


FIG. S5. Diagram showing the enlarged unit cell for the π -flux GMFT ansatz. There are eight tetrahedra in the unit cell, four on sublattice ‘A’, and four on sublattice ‘B’. The mean gauge field is defined on each spin site, and is represented by the circles and lines connecting tetrahedra. Black dashed lines and circles correspond to spin sites with $e^{i\tilde{A}} = 1$, and blue dotted lines and circles correspond to $e^{i\tilde{A}} = -1$. Open circles represent bonds pointing down into the page, and full circles are bonds pointing up out of the page.

The gauge field is assigned to the links between tetrahedra, or equivalently to each spin on the pyrochlore lattice. The configuration above enlarges the unit cell such that it now contains four ‘A’ sublattice tetrahedra, and four ‘B’ sublattice tetrahedra. Figure S5 presents a diagram of the unit cell, with sites labelled, and the value of the mean gauge field at each spin site indicated (see also Fig. S2. in the supplementary material for Ref. [5]).

The hard rotor constraint serves as a barrier to a tractable model due to the large number of Lagrange multipliers it introduces. There are several schemes one can use to relax this constraint, including introducing different fields to account for spinons and anti-spinons [6, 7], however we will here follow Ref. [5] and relax the hard rotor constraint on each site to a constraint on the average rotor length over all sites. We further impose that this mean rotor length be 2, and not 1, as this choice ensures that results are consistent with the classical Ising limit, as shown in [5]. We have then that:

$$\frac{1}{N} \sum_{\mathbf{r}_\alpha} \langle \Phi_{\mathbf{r}_\alpha}^\dagger \Phi_{\mathbf{r}_\alpha} \rangle = 2, \quad (\text{S39})$$

where N is the total number of ‘A’ tetrahedra sites on the pyrochlore lattice. The condition holds for both the ‘A’ and ‘B’ sublattices, and serves as a self consistency equation for a single Lagrange multiplier λ .

For the 0-flux phase, the Matsubara Green’s function can be written down from the GMFT action after taking the Fourier transform of the spinon fields in both imaginary time and space. In Matsubara frequency and momentum space, the Green’s function is given by:

$$G(\omega, \mathbf{k})_0 = \frac{2J_{yy}}{\omega^2 + \epsilon(\mathbf{k})_0^2}, \quad (\text{S40})$$

with

$$\epsilon(\mathbf{k})_0 = \sqrt{2J_{yy} \left(\lambda - J_\pm \left(\cos(k_x/2) \cos(k_y/2) + \cos(k_y/2) \cos(k_z/2) + \cos(k_z/2) \cos(k_x/2) \right) \right)}. \quad (\text{S41})$$

Taking the inverse Fourier transform, and analytically continuing to real times, the time ordered correlation function of spinon fields is given by:

$$\langle T\Phi^*(t, \mathbf{r})\Phi(t', \mathbf{r}') \rangle = \frac{1}{N} \sum_{\mathbf{k}} \frac{J_{yy}}{\epsilon(\mathbf{k})_0} e^{i\epsilon(\mathbf{k})_0|t-t'|} e^{-i\mathbf{k}\cdot(\mathbf{r}-\mathbf{r}')}. \quad (\text{S42})$$

For the π -flux phase, both the ‘A’ and ‘B’ sublattices have four sites per unit cell, and so the inverse Green’s function is a 4×4 matrix. For the choice of gauge used above, the inverse Green’s function for spinons on the ‘A’ and ‘B’ sublattices come out as:

$$G(\omega, \mathbf{k})_A^{-1} = \left(\frac{\omega^2}{2J_{yy}} + \lambda \right) \mathbb{1}_4 - \frac{J_{\pm}}{2} M; \quad G(\omega, \mathbf{k})_B^{-1} = \left(\frac{\omega^2}{2J_{yy}} + \lambda \right) \mathbb{1}_4 - \frac{J_{\pm}}{2} M^*, \quad (\text{S43})$$

where the matrix $M(\mathbf{k})$ is the following:

$$M = \begin{pmatrix} C_{yz} & C_{zx} - iS_{xy} & C_{xy} + iS_{zx} & -iS_{yz} \\ C_{zx} + iS_{xy} & -C_{yz} & -iS_{yz} & C_{xy} - iS_{zx} \\ C_{xy} - iS_{zx} & iS_{yz} & -C_{yz} & -C_{zx} - iS_{xy} \\ iS_{yz} & C_{xy} + iS_{zx} & -C_{zx} + iS_{xy} & C_{yz} \end{pmatrix}, \quad (\text{S44})$$

with $C_{\mu\nu} = \cos(k_{\mu}/2 + k_{\nu}/2)$ and $S_{\mu\nu} = \sin(k_{\mu}/2 - k_{\nu}/2)$. It can be shown that the matrix $M(\mathbf{k})$ satisfies $M(\mathbf{k})^2 = \xi^2 \mathbb{1}$, with

$$\xi(\mathbf{k}) = \sqrt{3 - \sin(k_x) \sin(k_y) - \sin(k_y) \sin(k_z) - \sin(k_z) \sin(k_x)}. \quad (\text{S45})$$

Using this, it can be verified that the Matsubara Green’s function for the ‘A’ sublattice in the π -flux phase is given by:

$$G(\omega, \mathbf{k})_A = \frac{1}{\left(\frac{\omega^2}{2J_{yy}} + \lambda \right)^2 - \left(\frac{J_{\pm}}{2} \right)^2 \xi(\vec{k})^2} \left(\frac{\omega^2}{2J_{yy}} + \lambda + \frac{J_{\pm}}{2} M \right). \quad (\text{S46})$$

The Green’s function for the ‘B’ sublattice is almost identical, just with the matrix M substituted for its complex conjugate.

Similarly taking the inverse Fourier transform, and analytically continuing to real times, we arrive at the following expression for the time ordered correlation functions in the π -flux phase:

$$\begin{aligned} \langle T\Phi^*(t, \mathbf{r})_s \Phi(t', \mathbf{r}')_r \rangle_A &= \frac{4}{N} \sum_{\mathbf{k}} \frac{J_y}{2} \left(\frac{1}{\epsilon(\mathbf{k})_+} \left(\delta_{s,r} - \frac{J_{\pm}}{|J_{\pm}|} \frac{M_{s,r}}{\xi} \right) e^{i\epsilon(\mathbf{k})_+|t-t'|} \right. \\ &\quad \left. + \frac{1}{\epsilon(\mathbf{k})_-} \left(\delta_{s,r} + \frac{J_{\pm}}{|J_{\pm}|} \frac{M_{s,r}}{\xi} \right) e^{i\epsilon(\mathbf{k})_-|t-t'|} \right) e^{-i\mathbf{k}\cdot(\mathbf{r}-\mathbf{r}')}, \end{aligned} \quad (\text{S47})$$

The corresponding expression for the ‘B’ sublattice again is the same but with M exchanged for its complex conjugate. Here we define the $\epsilon(\mathbf{k})_{\pm}$ as:

$$\epsilon(\mathbf{k})_{\pm} = \sqrt{2J_{yy} \left(\lambda \pm \frac{|J_{\pm}|}{2} \sqrt{3 - \sin(k_x) \sin(k_y) - \sin(k_y) \sin(k_z) - \sin(k_z) \sin(k_x)} \right)}. \quad (\text{S48})$$

Armed with the real space-time correlation functions, the mean rotor length conditions can be re-written in terms of sums over the Brillouin zones for the 0-flux and π -flux phases. In the 0-flux phase, the self consistency equation for λ is:

$$2 = \frac{1}{N} \sum_{\mathbf{k}} \frac{J_{yy}}{\epsilon(\mathbf{k})}, \quad (\text{S49})$$

and in the π -flux phase we find an analogous expression:

$$2 = \frac{4}{N} \sum_{\vec{k}} \frac{J_{yy}}{2} \left(\frac{1}{\epsilon(\mathbf{k})_{\pi,+}} + \frac{1}{\epsilon(\mathbf{k})_{\pi,-}} \right), \quad (\text{S50})$$

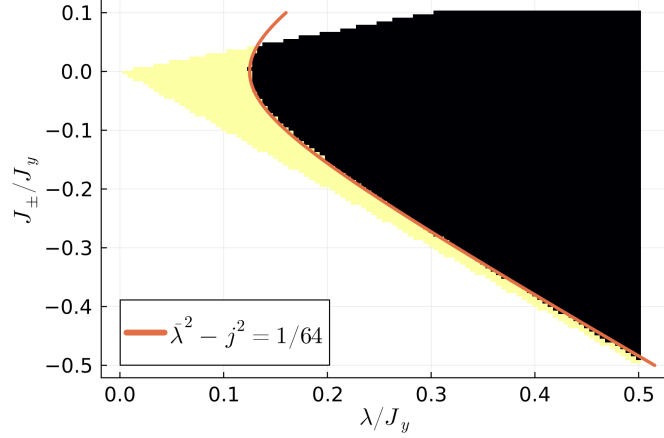


FIG. S6. Evaluation of the RHS of Eq. (S49) and Eq. (S50) as functions of $j = J_{pm}/J_{yy}$ and $\bar{\lambda}/J_{yy}$. The 0-flux condition is evaluated for positive j , and the π -flux for negative. These functions are less than 2 in the black region, and greater than 2 in the yellow region, with the desired relationship between j and $\bar{\lambda}$ then being the boundary between these regions. The red curve is the line $\lambda^2 - j^2 = \frac{J_{yy}^2}{64}$, which exactly follows the boundary.

Referring to the results of Ref. [5], the 0-flux phase is only stabilised for a certain range of positive J_{\pm} , and the π -flux phase only for negative J_{\pm} . Evaluating the conditions on λ numerically for all J_{\pm} where gapped spinon GMFT solutions exist, we find that following expression holds:

$$\lambda^2 - J_{\pm}^2 = \frac{J_{yy}^2}{64}, \quad J_{\pm} < J_{yy}/8^{3/2}. \quad (\text{S51})$$

Figure S6 presents the numerical results with the above relationship superimposed, and one can see essentially perfect agreement. For J_{\pm} greater than $J_{yy}/8^{3/2}$, no gapped spinon solutions exist, but the π -flux GMFT phase is well defined for arbitrarily large negative J_{\pm} .

Using the above results, one can now calculate the third-order response of QSI for both the 0- and π -flux GMFT phases. The desired susceptibility can be written in the following form:

$$\begin{aligned} \chi^{(3)}(t, t, t + \tau) = & \frac{\theta(t)\theta(\tau)}{2N} \sum_{j,l,m,n} [\text{Im} \{ \langle S_j^z(t + \tau) S_l^z(\tau) S_m^z(\tau) S_n^z(0) \rangle \} \\ & + \text{Im} \{ \langle S_j^z(\tau) S_l^z(\tau) S_m^z(t + \tau) S_n^z(0) \rangle \} + 2\text{Im} \{ \langle S_j^z(0) S_l^z(\tau) S_m^z(t + \tau) S_n^z(\tau) \rangle \}] \\ & \times (\mathbf{h} \cdot \mathbf{z}_j)(\mathbf{h} \cdot \mathbf{z}_l)(\mathbf{h} \cdot \mathbf{z}_m)(\mathbf{h} \cdot \mathbf{z}_n), \quad (\text{S52}) \end{aligned}$$

where the roman indices j, l, m, n run over all $4N$ spin sites, and $\mathbf{h} = \mathbf{H}/|\mathbf{H}|$. We can index these by running over all 'A' tetrahedra sites $\mathbf{r}_{i,A}$, and all spin sites connected to these tetrahedra indexed by $\mu_i = 0, 1, 2, 3$. Each S^z operator can be expanded in terms of spinon and gauge fields as:

$$S_{\mathbf{r}_A, \mathbf{r}_A + \mathbf{b}_\mu}^z = \frac{1}{4} \left\{ \Phi_{\mathbf{r}_A}^{\tau*} e^{i\bar{A}_{\mathbf{r}_A, \mathbf{r}_A + \mathbf{b}_\mu}} \Phi_{\mathbf{r}_A + \mathbf{b}_\mu}^\tau + \Phi_{\mathbf{r}_A + \mathbf{b}_\mu}^{\tau*} e^{-i\bar{A}_{\mathbf{r}_A, \mathbf{r}_A + \mathbf{b}_\mu}} \Phi_{\mathbf{r}_A}^\tau \right\}. \quad (\text{S53})$$

This can then be inserted into the expression for the non-linear susceptibility. Correlation functions of four fields can be Wick expanded, and the only non-vanishing terms are those with no correlation functions of fields on different sublattices.

Terms in the Wick expansion can be represented by Feynman diagrams, with edges corresponding to time-ordered correlators. All terms corresponding to diagrams that are not fully connected ultimately cancel out, and the only contributing diagrams are displayed in Fig. S7.

For the 0-flux phase, each edge of a Feynman diagram is associated with the \mathbf{k} -dependent correlation function $(J_{yy}/\epsilon(\mathbf{k}))_0 e^{i\epsilon(\mathbf{k})(t-t')}$, and each vertex with a function $V(\mathbf{k})$ defined as:

$$V(\mathbf{k}) = \sum_{\mu} e^{i\mathbf{k} \cdot \mathbf{b}_\mu} (\mathbf{h} \cdot \mathbf{z}_\mu). \quad (\text{S54})$$

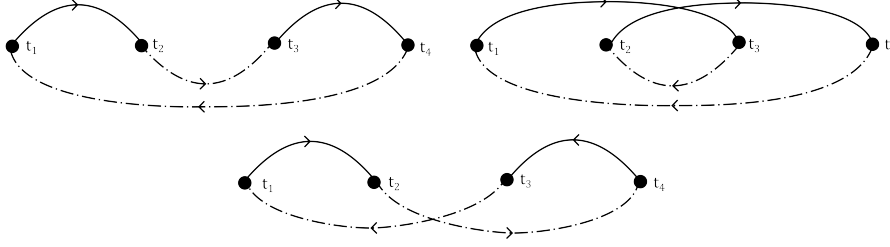


FIG. S7. Feynman diagrams contributing to the third order non-linear response. The direction of positive momentum is indicated by the arrow attached to each line. Spinons on the ‘A’ sublattice are represented with a full line, and those on the ‘B’ sublattice with a dashed line. Each diagram has a multiplicity of 2 in the full Wick expansion, corresponding to flipping the diagrams vertically. For the purpose of time ordering, t_4 appears first in the operator expansion, followed by t_3 , etc. The t_i are substituted for $0, \tau, t + \tau$ to evaluate the three different terms appearing in Eq. (S52).

At each vertex, as spinon moves from the ‘A’ sublattice to the ‘B’ sublattice or vice versa. When moving from ‘A’ to ‘B’, following the direction of positive momentum, the associated vertex factor is V , and when moving from ‘B’ to ‘A’ it is instead V^* .

In principle the theory produces for each diagram a copy with spinons and anti-spinons exchanged. However, including these sign swapped diagrams over-estimates response functions by a factor of two. To see this, consider acting on the true ground state with S^z to create a spinon-antispinon pair. The true ground state is some superposition of all classical ground states, and as such any given pseudo-spin S^y value is equally likely to be ± 1 . When acting with S^z , we create two spinons of equal and opposite sign, but the exact sign taken by each spinon depends on the sign of S^y , and so is entangled with the background spin configuration and is not uniquely defined. The GMFT ignores this entanglement, but maintains the spinon-antispinon symmetry, and so must double count the number of response pathways. To avoid over-counting the multiplicity of each diagram is divided by two.

Evaluating the sum over all valid diagrams, one arrives at the result:

$$\chi_0^{(3)} = -\frac{\theta(t)\theta(\tau)}{256N} \sum_{\mathbf{k}} \left(\frac{J_y}{\epsilon(\mathbf{k})_0} \right)^4 |V(\mathbf{k})|^4 \{-\sin(2\epsilon(\mathbf{k})_0(t+\tau)) + 2\sin(2\epsilon(\mathbf{k})_0(\tau)) + \sin(2\epsilon(\mathbf{k})_0(t-\tau))\}, \quad (\text{S55})$$

For the π -flux phase, we have an analogous construction, only with more complicated expressions for the internal lines and vertices of the Feynman diagrams. The internal lines are given by the time-ordered correlator defined in Eq. (S47) (or by its complex conjugate for time reversed paths). The vertex factors again include the geometrical couplings $(\mathbf{h} \cdot \mathbf{z}_\mu)$ and k dependent complex exponents, but these factors must now also correctly ‘knit’ the ‘A’ and ‘B’ sublattices together. As a result, the vertex factors are promoted to matrices, given in full by:

$$\begin{pmatrix} e^{i\mathbf{k} \cdot \mathbf{b}_0(\mathbf{h} \cdot \mathbf{z}_0) + e^{i\mathbf{k} \cdot \mathbf{b}_1(\mathbf{h} \cdot \mathbf{z}_1)} & e^{i\mathbf{k} \cdot \mathbf{b}_2(\mathbf{h} \cdot \mathbf{z}_2)} & e^{i\mathbf{k} \cdot \mathbf{b}_3(\mathbf{h} \cdot \mathbf{z}_3)} & 0 \\ e^{i\mathbf{k} \cdot \mathbf{b}_2(\mathbf{h} \cdot \mathbf{z}_2)} & e^{i\mathbf{k} \cdot \mathbf{b}_0(\mathbf{h} \cdot \mathbf{z}_0) - e^{i\mathbf{k} \cdot \mathbf{b}_1(\mathbf{h} \cdot \mathbf{z}_1)} & 0 & e^{i\mathbf{k} \cdot \mathbf{b}_3(\mathbf{h} \cdot \mathbf{z}_3)} \\ e^{i\mathbf{k} \cdot \mathbf{b}_3(\mathbf{h} \cdot \mathbf{z}_3)} & 0 & e^{i\mathbf{k} \cdot \mathbf{b}_0(\mathbf{h} \cdot \mathbf{z}_0) - e^{i\mathbf{k} \cdot \mathbf{b}_1(\mathbf{h} \cdot \mathbf{z}_1)} & -e^{i\mathbf{k} \cdot \mathbf{b}_2(\mathbf{h} \cdot \mathbf{z}_2)} \\ 0 & e^{i\mathbf{k} \cdot \mathbf{b}_3(\mathbf{h} \cdot \mathbf{z}_3)} & -e^{i\mathbf{k} \cdot \mathbf{b}_2(\mathbf{h} \cdot \mathbf{z}_2)} & e^{i\mathbf{k} \cdot \mathbf{b}_0(\mathbf{h} \cdot \mathbf{z}_0) + e^{i\mathbf{k} \cdot \mathbf{b}_1(\mathbf{h} \cdot \mathbf{z}_1)} \end{pmatrix}. \quad (\text{S56})$$

For vertices where the spinon moves from sublattice ‘B’ to sublattice ‘A’, the Hermitian conjugate of this matrix is instead required. Putting everything together, the full third order non-linear susceptibility for the π -flux phase can be written succinctly as:

$$\chi_\pi^{(3)}(t, t, t + \tau) = \frac{\theta(t)\theta(\tau)}{256N} \sum_{\mathbf{k}} \sum_{\{a_i\}=\pm 1} \left(\frac{J_{yy}}{2} \right)^4 \frac{F(\mathbf{k})_{a_1, a_2, a_3, a_4}}{\epsilon_{a_1} \epsilon_{a_2} \epsilon_{a_3} \epsilon_{a_4}} f(t, \tau, \{\epsilon_{a_i}\}). \quad (\text{S57})$$

In writing this expression we have separately indexed the two terms in the π -flux correlation function corresponding to the upper and lower bands using the indices $a_i = \pm 1$. The $F(\mathbf{k})$ functions are matrix

traces, and contain all of the time independent factors for each diagram, and are defined as:

$$F(\mathbf{k})_{a_1, a_2, a_3, a_4} = \text{Tr} \left\{ \left(1 - a_1 \frac{J_{\pm}}{|J_{\pm}|} \frac{M}{\xi} \right) V^{\dagger} \left(1 - a_2 \frac{J_{\pm}}{|J_{\pm}|} \frac{M^*}{\xi} \right) V \left(1 - a_3 \frac{J_{\pm}}{|J_{\pm}|} \frac{M}{\xi} \right) V^{\dagger} \left(1 - a_4 \frac{J_{\pm}}{|J_{\pm}|} \frac{M^*}{\xi} \right) V \right\}. \quad (\text{S58})$$

The time dependent factors encapsulated in the function f are then in full:

$$\begin{aligned} f(t, \tau, \{a_i\}) = & 2 \sin((\epsilon_{a_3} + \epsilon_{a_4})t + (\epsilon_{a_1} + \epsilon_{a_4})\tau) + \sin((\epsilon_{a_1} - \epsilon_{a_2})t + (\epsilon_{a_1} + \epsilon_{a_4})\tau) + 2 \sin((\epsilon_{a_1} - \epsilon_{a_2})t - (\epsilon_{a_3} + \epsilon_{a_4})\tau) \\ & + \sin((\epsilon_{a_2} + \epsilon_{a_3})t + (\epsilon_{a_1} + \epsilon_{a_4})\tau) + \sin((\epsilon_{a_4} - \epsilon_{a_3})t + (\epsilon_{a_1} + \epsilon_{a_4})\tau) + 2 \sin((\epsilon_{a_4} - \epsilon_{a_3})t - (\epsilon_{a_2} + \epsilon_{a_3})\tau) \\ & - \sin((\epsilon_{a_2} + \epsilon_{a_3})t - (\epsilon_{a_1} + \epsilon_{a_4})\tau) - 2 \sin((\epsilon_{a_2} + \epsilon_{a_3})t + (\epsilon_{a_3} + \epsilon_{a_4})\tau). \quad (\text{S59}) \end{aligned}$$

Note however that the rephasing signal part of the response is generated only by the term: $-\sin((\epsilon_{a_2} + \epsilon_{a_3})t - (\epsilon_{a_1} + \epsilon_{a_4})\tau)$.

-
- [1] M. Udagawa and R. Moessner, Phys. Rev. Lett. **122**, 117201 (2019).
 - [2] C. Wei and S. H. Curnoe, "Symmetry considerations in exact diagonalization: spin-1/2 pyrochlore magnets," (2023), arXiv:2309.10670 [cond-mat.str-el].
 - [3] Y. Wan and N. P. Armitage, Phys. Rev. Lett. **122**, 257401 (2019).
 - [4] O. Hart and R. Nandkishore, Phys. Rev. B **107**, 205143 (2023).
 - [5] F. Desrochers and Y. B. Kim, Phys. Rev. Lett. **132**, 066502 (2024).
 - [6] Z. Hao, A. G. R. Day, and M. J. P. Gingras, Phys. Rev. B **90**, 214430 (2014).
 - [7] F. Desrochers and Y. B. Kim, "Finite temperature dynamics in 0-flux and π -flux quantum spin ice: Self-consistent exclusive boson approach," (2024), arXiv:2401.09551 [cond-mat.str-el].